

Magnification of Photometric LRGs by Foreground LRGs and Clusters in SDSS

Anne H. Bauer^{1*}, Enrique Gaztañaga¹, Pol Martí², Ramon Miquel^{2,3}

¹*Institut de Ciències de l'Espai, CSIC/IEEC, E-08193 Bellaterra, Spain*

²*Institut de Física d'Altes Energies, Universitat Autònoma de Barcelona, E-08193 Bellaterra, Spain*

³*Institució Catalana de Recerca i Estudis Avançats, E-08010 Barcelona, Spain*

7 January 2018

ABSTRACT

The magnification effect of gravitational lensing is a powerful probe of the distribution of matter in the universe, yet it is frequently overlooked due to the fact that its signal to noise is smaller than that of lensing shear. Because its systematic errors are quite different from those of shear, magnification is nevertheless an important approach with which to study the distribution of large scale structure. We present lensing mass profiles of spectroscopic luminous red galaxies (LRGs) and galaxy clusters determined through measurements of the weak lensing magnification of photometric LRGs in their background. We measure the change in detected galaxy counts as well as the increased average galaxy flux behind the lenses. In addition, we examine the average change in source color due to extinction by dust in the lenses. By simultaneously fitting these three probes we constrain the mass profiles and dust-to-mass ratios of the lenses in six bins of lens richness. For each richness bin we fit an NFW halo mass, brightest cluster galaxy (BCG) mass, second halo term, and dust-to-mass ratio. The resulting mass-richness relation is consistent with previous analyses of the catalogs, and limits on the dust-to-mass ratio in the lenses are in agreement with expectations. We explore the effects of including the (low signal-to-noise) flux magnification and reddening measurements in the analysis compared to using only the counts magnification data; the additional probes significantly improve the agreement between our measured mass-richness relation and previous results.

Key words: gravitational lensing:weak – galaxies:clusters:general – methods:data analysis

1 INTRODUCTION

Gravitational lensing, the deflection of photons by changes in gravitational potential, modifies the observed brightness and shape of sources behind massive objects. Lensing is therefore a powerful technique to measure the distribution of matter, as its effects on source flux and shape are directly due to the mass along the line of sight.

Galaxy clusters are extremely massive collapsed systems and act as powerful gravitational lenses. As the peaks of the matter density distribution, they constitute sensitive probes of cosmology (e.g., Mantz et al. 2008; Rozo et al.

2010). To constrain cosmology using the abundance of galaxy clusters, one must have accurate knowledge of the clusters' masses; gravitational lensing provides a natural way to constrain these masses.

Traditionally, weak gravitational lensing has been measured using shear: the distortion of the shape of galaxies behind a lens. Shear is technically very difficult to measure, requiring high-quality, resolved images of distant galaxies; as a result, increasing attention is being paid to the magnification effects of weak lensing. The signal-to-noise of the magnification of source galaxies behind a lens is typically smaller than that of the galaxies' shear (see Schneider et al. 2000, equ. 7). The exact ratio depends on the shape of the lens mass profile and the sources' lensing sensitivity α_c , defined

* E-mail: bauer@ieec.uab.es

below in equation 15, but for a singular isothermal sphere lens and a given number of sources with the same α_c as in this work, the signal-to-noise of the magnification effect is about a factor of three smaller than that of lensing shear. In magnification analyses, however, one can include unresolved (fainter, higher-redshift) galaxies in the source sample and thereby reduce the statistical noise in the result. In addition, it is important to study magnification even if its statistical errors are larger than those of shear, as the systematic effects that complicate the measurement of magnification (e.g., photometric calibration homogeneity, detection completeness) are typically different from those afflicting shear (e.g., image resolution and seeing, intrinsic alignments).

Magnification is a fundamentally different lensing probe from shear in that its effects are proportional to the lens mass profile itself, as opposed to the change in the mass distribution as in the case of shear. Magnification, in the weak lensing regime, measures the divergence of the gradient of the lensing deflection potential (the scalar convergence κ), while the shear is a polar given by the second derivatives of the potential. As a result, certain profile shapes (e.g. a point mass, or the profile of a second halo term) appear very differently to the two probes, allowing the two lensing signals to provide complementary information. In addition, shear measurements suffer from the “mass-sheet degeneracy”, whereby a uniform sheet of mass is undetectable. This degeneracy complicates the use of shear to calibrate the masses of lenses, as the point where the shear signal falls to zero may not be the point where the mass overdensity falls to zero. The degeneracy can be practically overcome by using large areas of sky over which one may assume that cosmic variance does not cause a significant mass sheet. Still, the problem is formally eliminated by using magnification measurements, where a mass sheet causes a measurable effect. Magnification is therefore important in ensuring the proper normalization of mass profiles in lensing analyses.

Most studies of weak lensing magnification have measured “magnification bias”: the change in detection rate of a magnified source population in a flux-limited survey due to the combination of increased observed object flux and decreased solid angle behind a lens. Depending on how the number count distribution of the source sample changes with luminosity, magnification bias can lead to an increase or decrease in counts. Other studies have measured the increase in measured flux (Ménard et al. 2010) and size (Schmidt et al. 2012) in lensed sources, and how these lensed quantities affect scaling relations such as the fundamental plane (Sonnenfeld et al. 2011; Huff & Graves 2011) and the quasar variability-luminosity relation (Bauer et al. 2011, 2012). Studying another consequence of lensing magnification, Coupon et al. (2013) measured the change in the distribution of spectroscopic redshifts measured behind lenses.

When measuring lensing magnification it is essential to minimize redshift overlap in the source and lens samples, as physical correlations between the source and lens objects would lead to an increase of objects in the source catalog as a function of decreasing angular distance from

objects in the lens catalog. Depending on the properties of the source catalog, magnification can induce a positive or negative change in source number count density (see Section 2.2). Redshift overlap between the catalogs can therefore mimic or counteract the true lensing signal, with an amplitude much larger than that of magnification. Because of this, photometric source samples in magnification analyses have consisted of objects with very reliable estimates of high redshifts, such as quasars (Gaztañaga 2003; Scranton et al. 2005; Ménard et al. 2010), Lyman break galaxies (Van Waerbeke et al. 2010; Hildebrandt et al. 2011, 2013; Morrison et al. 2012; Ford et al. 2012, 2013), and galaxies in targeted fields with unusually deep, high-quality photometry (Schmidt et al. 2012; Umetsu et al. 2012). In this work we use a sample of luminous red galaxies (LRGs) for which we have well-measured photometric redshifts. These galaxies are at a redshift lower than is typical in magnification analyses ($0.5 < z < 0.6$), but as we have good knowledge of the objects’ true redshift distribution we can quantify any contamination with our lens samples.

Although gravitational lensing by a massive object increases a source’s observed flux, absorption by dust associated with the same lens can do the opposite. Dust absorption also causes a reddening of the source flux. Because lensing is achromatic, it is possible to disentangle the two effects and study both the lens mass and dust content using multi-color data (Ménard et al. 2010).

We measure the weak lensing magnification of the photometric MegaZ sample of LRGs (Thomas et al. 2010) from the Sloan Digital Sky Survey Data Release 7 (Abazajian et al. 2009), due to LRG (Cabré & Gaztañaga 2009) and galaxy cluster (Wen et al. 2012) lenses in the foreground. Our lens samples are spectroscopic, with redshifts from 0.1 to 0.4. The sources have photometric redshifts between 0.5 and 0.6. We simultaneously measure the counts increase and average flux increase due to lensing, as well as any reddening due to dust in the lenses. Using these probes we constrain the mass profiles of the lenses as modeled as a dark matter halo, brightest cluster galaxy, and second halo term, and also put limits on the dust-to-mass ratio in the lenses. We fit such lens models in each of six bins in lens richness: one bin for the LRG sample, and five for the cluster catalog.

Throughout the analyses we assume the cosmological parameters $H_0 = 70 \text{ km s}^{-1} \text{ Mpc}^{-1}$, $\Omega_m = 0.3$, $\Omega_\Lambda = 0.7$, $\sigma_8 = 0.807$, $n_s = 0.961$.

2 LENSING MAGNIFICATION

The deflection of light by a gravitational lens causes sources in the lens’ background to appear brighter than they intrinsically are. This is due to the apparent geometrical stretching of space behind the lens, coupled with the fact that lensing conserves the sources’ apparent surface brightness. The magnification μ can be calculated from the Jacobian matrix A of the lensing distortion:

$$\mu = \frac{1}{\det \mathcal{A}} = \frac{1}{(1 - \kappa)^2 - |\gamma|^2} \quad (1)$$

where κ is the convergence and γ is the shear induced by the lens. For a general description of gravitational lensing physics, see, e.g., Schneider et al. (2004).

In the limit of weak lensing, where κ and γ are small, equation 1 can be approximated by

$$\mu \approx 1 + 2\kappa. \quad (2)$$

The dimensionless convergence κ can be expressed as the surface mass density Σ divided by the critical surface mass density of the lensing system Σ_{cr} :

$$\kappa \equiv \frac{\Sigma}{\Sigma_{cr}} \quad (3)$$

with

$$\Sigma_{cr} = \frac{c^2}{4\pi G} \frac{D_s}{D_d D_{ds}} \quad (4)$$

where D_d , D_s , D_{ds} are the angular diameter distances from the observer to the lens, the observer to the source, and from the lens to the source, respectively.

Because we typically deal with fluctuations in magnification around $\mu = 1$, it is convenient to define the relative magnification δ_μ :

$$\delta_\mu \equiv \mu - 1 \approx 2\kappa \quad (5)$$

where the latter approximation holds in the weak lensing limit.

One typically measures magnification by comparing properties of lensed objects to those of a large sample. In this analysis, we measure the change in average magnitude of sources behind lenses as well as the change in detection rate (counts) of the sources.

2.1 Magnitudes

The apparent magnitude of a single object i is changed by magnification according to:

$$\delta_{m_i}(\mu) = -\frac{2.5}{\ln(10)} \delta_\mu. \quad (6)$$

The corresponding average change in magnitude for a population of galaxies has an additional term due to the change in the sample's limiting magnitude m_* in a magnified region (i.e. more galaxies are brought above the magnitude limit by the magnification effect):

$$\delta_{\bar{m}}(\mu) = \left(\frac{d\bar{m}}{dm_i} \frac{dm_i}{d\mu} + \frac{d\bar{m}}{dm_*} \frac{dm_*}{d\mu} \right) \delta_\mu \quad (7)$$

$$= -\frac{2.5}{\ln(10)} \left(1 - \frac{d\bar{m}}{dm_*} \right) \delta_\mu \quad (8)$$

where in the last equality we have used equation 6. The change in magnitude of a lensed sample is then

$$\delta_m(\mu) = \alpha_m \delta_\mu \quad (9)$$

where we have introduced α_m as

$$\alpha_m \equiv \frac{2.5}{\ln(10)} \left(-1 + \frac{d\bar{m}(m_*)}{dm_*} \right). \quad (10)$$

We note that α_m is related to C_s defined in Ménard et al. (2010) via $\alpha_m = (-2.5/\ln(10)) C_s$, with both expressing the change in mean magnitude of a sample due to a variation of the sample magnitude limit.

Combining equations 2, 3, 5, and 9, we find how the surface mass density of the lens can be calculated from $\delta_m(\mu)$. As this surface mass density is determined from the lensing-induced fluctuation in magnitudes, we call it Σ_m :

$$\Sigma_m = \frac{\delta_m(\mu) \Sigma_{cr}}{2\alpha_m}. \quad (11)$$

2.2 Counts

The number of detections in a flux-limited survey is altered by gravitational lensing because of two effects. First, magnification increases the area behind lenses, and this decreases the number of sources:

$$\delta_c(\text{area}) \equiv \frac{dn}{n} = -\delta_\mu \quad (12)$$

where n is the number density of sources.

Second, magnification also changes the object fluxes, as discussed above. This causes objects that are intrinsically fainter than the survey's magnitude limit m_* to appear brighter, and therefore be detected:

$$\begin{aligned} \delta_c(\text{flux}) &\equiv \frac{dn}{d\mu} \frac{\delta_\mu}{n} \\ &= \frac{2.5}{\ln(10)} \frac{dn}{dm_*} \frac{\delta_\mu}{n} \\ &= -2.5 \frac{d}{dm_*} (\log_{10} n) \delta_\mu \end{aligned} \quad (13)$$

The total lensing-induced change in number counts $\delta_c(\mu)$ is the sum of these two components, and so we define

$$\delta_c(\mu) = \delta_c(\text{flux}) + \delta_c(\text{area}) = \alpha_c \delta_\mu \quad (14)$$

where

$$\alpha_c \equiv 2.5 \frac{d}{dm_*} \log_{10} n_o(< m_*) - 1.0 \quad (15)$$

with n_o the unlensed source number density. α_c therefore relates the lensing-induced change in number counts $\delta_c(\mu)$ to the relative magnification δ_μ .

Analogously to equation 11, we can define Σ_c , the surface mass density of a lens as calculated by the lensing-induced change in counts of a sample of sources:

$$\Sigma_c = \frac{\delta_c(\mu)\Sigma_{cr}}{2\alpha_c}. \quad (16)$$

3 DUST EXTINCTION

Dust in the lenses absorbs light from the background sources, creating an extinction effect that can be of comparable amplitude with the flux changes due to lensing magnification. Dust mass appears to trace total halo mass (Ménard et al. 2010; Hildebrandt et al. 2013), which causes the two signals to have similar radial dependence. Fortunately, dust extinction is wavelength dependent while gravitational lensing is achromatic, allowing us to use multicolor photometry of the sources to disentangle the two effects.

The change in V-band magnitude of a source due to dust extinction is

$$\delta_{m_r(V)} = A_V = R_V E(B - V). \quad (17)$$

The total extinction A_V denotes the V magnitude change due to dust extinction. The relative extinction $E(B - V)$ quantifies how the extinction changes the object's $B - V$ color. The two can be related through the parameter R_V , which depends on the physical properties of the dust such as the typical grain size. R_V is commonly taken to be about 3, as observed for interstellar dust in our Galactic disk and the small and large Magellanic clouds (SMC and LMC, respectively). We take $R_V = 2.93$, as observed for the SMC.

The relative extinction $E(B - V)$ is equal to the change in color, $\Delta(m_B - m_V)$. In fact, we use the color ($m_g - m_i$) of the sources to measure the reddening, as those bands are measured by SDSS and this color has larger signal to noise than the difference between closer filters such as g and r or r and i . To relate the observed source color fluctuations to the amount of dust in the lenses, we must convert the observed $\Delta(m_g - m_i)$ to $\Delta(m_B - m_V)$ in the lens rest frame. We do this by assuming the SMC dust model from Pei (1992), which parameterizes the color dependence of extinction, and by using a template spectrum for the source LRGs. As discussed in Martí et al. (2013) and described in section 6.1, BPZ was run on the MegaZ source sample using CWW templates of the LePhare library.¹ The majority of the galaxies were matched to the LRG template `E11.01.sed`, which we therefore assume to be representative of the sample. With these models we can relate observed ($m_g - m_i$) to lens rest frame ($m_B - m_V$), to absolute extinction A_V in the lens frame, and to observed extinction A_i .

¹ The templates can be found in the folder `/lephare.dev/sed/GAL/CE_NEW/` of the LePhare package at http://www.cfht.hawaii.edu/~arnouts/LEPHARE/DOWNLOAD/lephare_dev_v2.2.tar.gz

To relate the extinction in the lens, A_V , to the total lens surface mass density Σ , we must assume the opacity of the dust K_{ext} that relates the dust's absorption cross section to its mass and depends on the dust grain composition. We take $K_{\text{ext}} = 1.54 \times 10^4 \text{cm}^2 \text{g}^{-1}$, following Ménard et al. (2010), from the SMC dust model in Weingartner & Draine (2001). If we assume a constant dust-to-mass ratio Γ in the lenses, then

$$\Sigma = \frac{\ln(10)}{2.5} \frac{A_V}{\Gamma \times K_{\text{ext}}}. \quad (18)$$

4 OBSERVABLES

Both lensing and dust extinction contributions must be taken into account when interpreting the measured fluctuations in object counts and magnitudes.

4.1 Counts

The fluctuation in observed counts due to lensing and extinction in a flux-limited survey can be written, in an elaboration of equation 14, as

$$\delta_c \equiv \frac{n}{\bar{n}} - 1 = \alpha_c \delta_\mu - \frac{\ln(10)}{2.5} (\alpha_c + 1) A_i. \quad (19)$$

The factor $(\alpha_c + 1)$ relates the magnitude change in m_* to the observed number of counts, while the term $\ln(10)/2.5$ results from the derivative of the base 10 logarithm in α_c . The subscript i in the extinction A_i refers to the fact that we measure changes in sources' i -band magnitudes.

Here n and \bar{n} are the observables: n is the number count density of objects in a given region, while \bar{n} is the mean number density of counts over the sky, which is used as an observable approximation to the unlensed number count density n_o .

4.2 Magnitudes

The average magnitude of a set of galaxies, compared to the magnitude averaged over the whole sky, can be written as:

$$\delta_m \equiv m - \bar{m} = \alpha_m \delta_\mu - \frac{\ln(10)}{2.5} \alpha_m A_i. \quad (20)$$

Because extinction and lensing both affect only the measured flux (i.e. there is no geometrical contribution as in the case of number counts), α_m affects both terms on the right hand side in the same way. The factor of $\frac{\ln(10)}{2.5}$ appears as a conversion factor because A_i is in units of magnitudes while δ_μ is unitless.

4.3 Conversion to Surface Mass Density

The surface mass density of the lens, taking into account both lensing and extinction, is analogous to equations 11

and 16 and has the same form in the case of counts and magnitudes observables:

$$\Sigma = \frac{\delta_{c,m}\Sigma_{cr}}{2\alpha_{c,m}}. \quad (21)$$

This implies that the surface mass density Σ can be obtained by applying a dust correction to Σ_m or Σ_c :

$$\Sigma = \Sigma_m - \frac{\ln(10)}{2.5} \frac{A_i \Sigma_{cr}}{2} \quad (22)$$

$$\Sigma = \Sigma_c - \frac{\ln(10)}{2.5} \frac{\alpha_c + 1}{\alpha_c} \frac{A_i \Sigma_{cr}}{2} \quad (23)$$

5 LENS MODELING

5.1 Main Halo

We model the dark matter halo, comprising the majority of the mass in the lens, as an NFW profile (Navarro et al. 1997):

$$\rho(r) = \frac{\delta_c \rho_{\text{crit}}}{(r/r_s)[1 + (r/r_s)]^2} \quad (24)$$

where c is the concentration parameter of the profile, $\delta_c = \frac{200}{3} \frac{c^3}{\ln(1+c) - c/(1+c)}$, and $r_s = R_{200}/c$. The total mass inside R_{200} is M_{200} . ρ_{crit} is the critical density of the universe at the redshift of the cluster.

The concentration of haloes has been seen to vary inversely with mass and redshift. We assume the relation measured in Mandelbaum et al. (2008):

$$c(M_{200}, z) = \frac{4.6}{1+z} \left(\frac{M_{200}}{1.56 \times 10^{14} h^{-1} M_{\odot}} \right)^{-0.13}. \quad (25)$$

The surface mass density profile Σ of an NFW lens can be calculated analytically, as given in Schneider et al. (2004).

We take M_{200} , the mass of the halo, to be the single free parameter in the model for the main halo.

5.1.1 Halo Miscentering

The centers of massive haloes are difficult to identify. Typically, the stated center of a galaxy cluster is chosen as the location of the brightest cluster galaxy (BCG). In some cases, the BCG may be offset from the true halo center. More often, the BCG is misidentified. Such errors in the determination of the halo center will lead to errors in the stacked halo profile, in particular making the stacked profile shallower than expected. Johnston et al. (2007) studied this problem in detail using simulations, resulting in a mass-dependent probability that a cluster is offset from its true center by a given amount. We implement this prescription in our NFW model of cluster haloes by using a composite halo profile that includes a contribution from miscentered haloes according to the probability and radial offsets given in Johnston et al.

(2007). This contribution makes the halo profile shallower, although not significantly given the measurement errors in our data.

We note that the miscentering prescription we implement is calibrated to match the behavior of a cluster catalog with a different selection technique from Wen et al. (2012). Furthermore, there are hints that the modeled miscentering is overestimated (Mandelbaum et al. 2008). We use the prescription as an example of the effects of miscentered haloes in the catalog, since we do expect a significant level of miscentering in any cluster sample, particularly when the center is identified as the location of the BCG as in both Johnston et al. (2007) and Wen et al. (2012). We examine the effects of including miscentering in our model in section 8.4.3.

5.2 BCG

We model the brightest cluster galaxy (BCG) of the halo as a cuspy profile defined similarly to equation 24:

$$\rho(r) = \frac{\delta_c \rho_{\text{crit}}}{(r/r_s)^{\gamma} [1 + (r/r_s)^2]^{(n-\gamma)/2}} \quad (26)$$

with $(\gamma, n) = (2, 4)$. This profile has steeper inner and outer slopes than the NFW profile, which is similar to equation 26 with $(\gamma, n) = (1, 3)$. We note that in lensing shear analyses of massive haloes the BCG has typically been modeled simply as a point mass (e.g. Johnston et al. 2007). This is unfeasible in the case of magnification modeling, where the observable is related to κ rather than the change in κ .

In our model, we fit for M_{200} of the BCG halo profile; as with the NFW profile, M_{200} is the mass enclosed in $R_{200} = r_s c$. For the BCG we again use the mass-concentration relation given in equation 25.

5.3 Second Halo Term

At large radii we expect to see lensing signal from haloes neighboring the main one. To calculate this second halo term we follow the procedure in Mandelbaum et al. (2005) to calculate the power spectrum of the second halo term using the NFW profile (whose Fourier transform y_{dm} is given analytically in Scoccimarro et al. 2001), the linear power spectrum P_{lin} (as calculated by the code NICA EA²), and a bias b of the lens:

$$P(k) = b P_{\text{lin}}(k, z) \int f(\nu) d\nu b(\nu) y_{\text{dm}}(k, M) \quad (27)$$

The functions $b(\nu)$ and $f(\nu)$ are the bias and mass functions derived using the spherical collapse formalism (following Mandelbaum et al. 2005; see Press & Schechter 1974; Sheth & Tormen 1999).

The Fourier transform of $P(k)$ yields $\xi_{\text{nfw, dm}}$, the cross-correlation between the lens halo and the neighboring dark

² <http://www2.iap.fr/users/kilbinge/nicaea/>

matter. Integrating along the line of sight produces the projected mass density Σ of the second halo term:

$$\Sigma(R) = \bar{\rho} \int \xi_{\text{nfw, dm}} [(R^2 + \chi^2)^{1/2}] d\chi \quad (28)$$

where $\bar{\rho}$ is the mean density of the universe at the redshift of the halo.

We fit for the lens bias b as the free parameter in the second halo term.

6 DATA

6.1 Sources

Our source sample is the MegaZ catalog of luminous red galaxies (LRGs) (Thomas et al. 2010) color-selected from the Sloan Digital Sky Survey (SDSS) Data Release 7 (Abazajian et al. 2009). The catalog contains 1,120,745 LRGs with photometric redshifts between 0.4 and 0.8, over a sky area of 7700 square degrees. For this study we use a subset of 572,900 galaxies with photometric redshift between 0.5 and 0.6 with deVaucouleurs i magnitude brighter than 19.8. We can quantify the accuracy of the photometric redshifts of this subsample because the galaxies have the same selection criteria as the spectroscopic 2SLAQ catalog (Cannon et al. 2006). Precise understanding of the redshift distribution $N(z)$ of the source sample is essential, as physical overlap between the sources and the lenses leads to a spurious lensing signal (see section 8.4.1). We use photometric redshifts for the sample calculated using the BPZ code (Benítez 2000) as discussed in Martí et al. (2013). The $N(z)$ of the photo- z bin 0.5-0.6 can be fit well by a sum of four Gaussian distributions, in order to parameterize accurately the shape of the peak and both high and low redshift tails. Fitting 3 parameters per Gaussian distribution, including covariance between the 12 parameters, yields a $\chi^2 = 23.4$ for 18 degrees of freedom; the best fit is shown in black in Figure 1.

We use the deVaucouleurs i magnitude to measure δ_m , and the model magnitudes g and i to measure color. The SDSS data, as published in the MegaZ catalog, have been calibrated to the 2% level⁴; we therefore add a systematic uncertainty of 2% to the magnitude and color measurements, on top of the jackknife uncertainties that constitute our primary error analysis. This is typically insignificant for the Σ_m measurements, but is large compared to the amplitude of the measured reddening of the sources.

The number of source galaxies versus deVaucouleurs i magnitude is shown in Figure 2. Measurements of α_c and α_m for the MegaZ sample are shown in Figure 3, versus the chosen limiting magnitude cut in de Vaucouleurs i . For the analysis we choose $i < 19.8$ because this corresponds to the faint limit of the 2SLAQ photometric redshift calibration

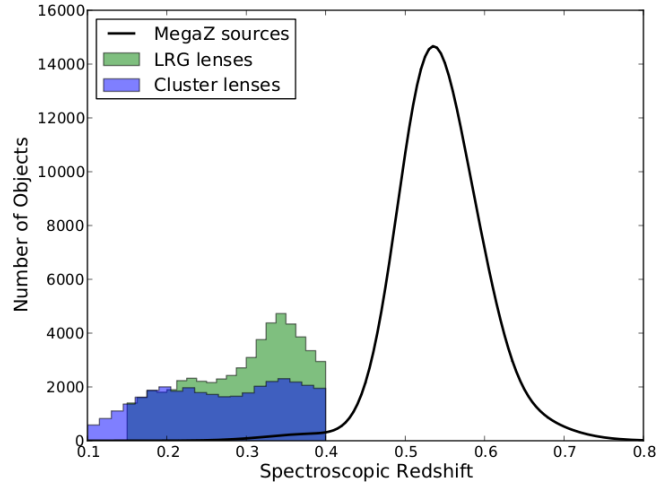


Figure 1. Redshift distributions of the LRG lenses (green), cluster lenses (blue), and MegaZ sources (black). The MegaZ curve is a fit using a subset of the data with spectroscopic redshifts; see text for details.

sample; the MegaZ catalog extends to $i = 20$. The distribution of the catalog number counts versus magnitude is modeled using kernel density estimation. The uncertainties on $\alpha_{c,m}$ are fundamentally uncertainties on the histogram shown in Figure 2, which can be caused by Poisson error, magnitude measurement error, or intrinsic variations in the number of objects per magnitude across the sky due to the presence of large scale structure. We estimate these errors on $\alpha_{c,m}$ by jackknife resampling in 133 regions over the survey area. In order to incorporate these measurement errors into our analyses, we include α_c and α_m as fit parameters in our analysis but constrain them with Gaussian priors around the best-fit values of 0.656 and -0.219, with 1σ errors of 12% and 2%, respectively. Note that α_m is much better constrained than α_c due to the smaller intrinsic correlation of galaxy magnitudes compared to galaxy positions.

6.2 Lenses

6.2.1 Cluster Catalog

We use the catalog of galaxy clusters presented in Wen et al. (2012), which are selected using photometric redshift measurements from SDSS data release 3 (Abazajian et al. 2005). For our cluster lens sample we take the subset of 28,617 clusters with spectroscopic redshift identifications⁵ z_{spec} between 0.1 and 0.4. The redshift distribution is shown in blue in Figure 1. We divide the sample into 5 bins of richness, shown as bins 1-5 in Table 1.

⁴ <http://www.sdss.org/dr7/algorithms/fluxcal.html>

⁵ http://zmtt.bao.ac.cn/galaxy_clusters/

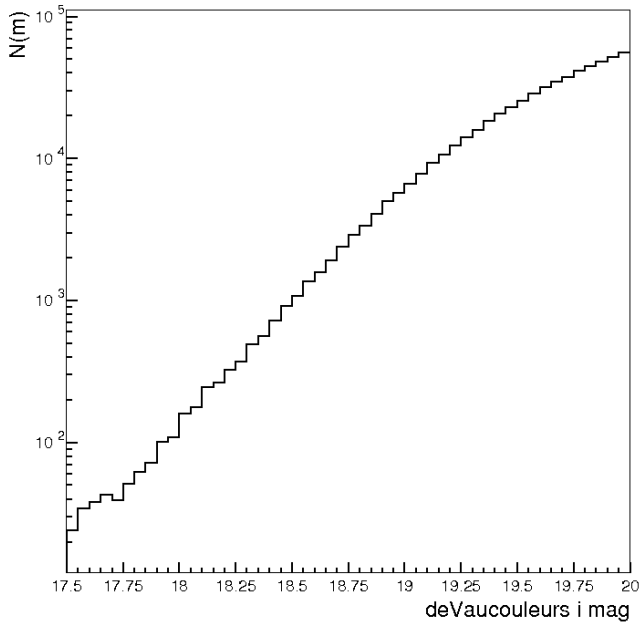


Figure 2. Number of MegaZ galaxies with redshift 0.5-0.6, versus deVaucouleurs i mag. For the analysis the cut is chosen at $i_{deV} = 19.8$.

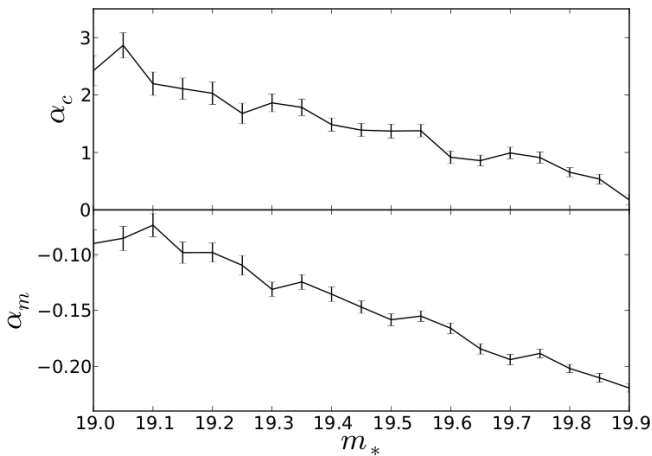


Figure 3. α_c (top) and α_m (bottom) versus the limiting magnitude cut m_* on the MegaZ catalog. For the analysis the cut is chosen at $i_{deV} = 19.8$.

6.2.2 LRGs

We also study a spectroscopic sample of luminous red galaxies (LRGs) identified in SDSS. This is the sample selected in Cabré & Gaztañaga (2009) using magnitude, color, and surface brightness cuts from SDSS data release 6 (Adelman-McCarthy et al. 2008). Of the 73,981 LRGs with redshifts between 0.1 and 0.4, 10% match with cluster catalog members within a radius of $10''$. We use as our LRG lens sample the remaining 66,613 galaxies and list them as

Richness Bin	Richness N	# Lenses
0	<12	66613
1	12-17	12270
2	18-25	9765
3	26-40	4649
4	41-70	1638
5	71-220	295

Table 1. Richness bin limits, and number of lenses per bin. Bins 1-5 constitute the cluster sample, while bin 0 corresponds to the spectroscopic LRG sample.

richness bin 0 in Table 1, with richness less than 12. Their spectroscopic redshift distribution is shown in green in Figure 1.

6.3 Spatial Mask

When calculating spatial fluctuations in the source detection rate, it is essential to use an accurate mask of the survey footprint. We generate a mask in Healpix format (Górski et al. 2005) with resolution $N_{\text{side}}=8192$, corresponding to pixel size of 26 arc seconds. When counting detections in an annulus around a lens, we query the mask for pixel centers within the annulus and correct our counts by the fraction of masked pixels in the annulus area. The relevant mask for the analysis is that of the MegaZ sources, as those are the objects for which we calculate the average density and spatial fluctuations. The LRG and cluster catalog cover similar footprints to the MegaZ, as all three are drawn from SDSS data. The cluster catalog includes additional area in the southern galactic cap that is not used in this analysis, as it does not overlap with the MegaZ footprint.

We calculate the mask for the MegaZ catalog in a two-step process. First, we use the Healpix mask for the sample, with $N_{\text{side}}=1024$, that is provided with the catalog. This mask provides the overall footprint of the survey. Second, we mask regions of poor SDSS data quality inside the footprint by examining the density of stars in the area. We download from the SDSS CasJobs server⁶ all stars in the region brighter than r magnitude 19.6. A map of this dense stellar catalog clearly shows regions with systematically lower density, likely due to poor observing conditions. We generate a star map with $N_{\text{side}}=512$ and mark pixels as bad if they include fewer than 8 stars. This cut removes areas such as a long line in the SDSS driftscan direction at high right ascension and intermediate declination, as well as some rectangular regions at high declination and negative right ascension. The cut also eliminates small disjoint regions at high galactic latitudes that have few stars due to statistical fluctuations. As these regions are spatially uncorrelated with the positions of gravitational lenses, masking them will not bias our analysis. The intersection of the resulting star mask

⁶ <http://casjobs.sdss.org/CasJobs/>

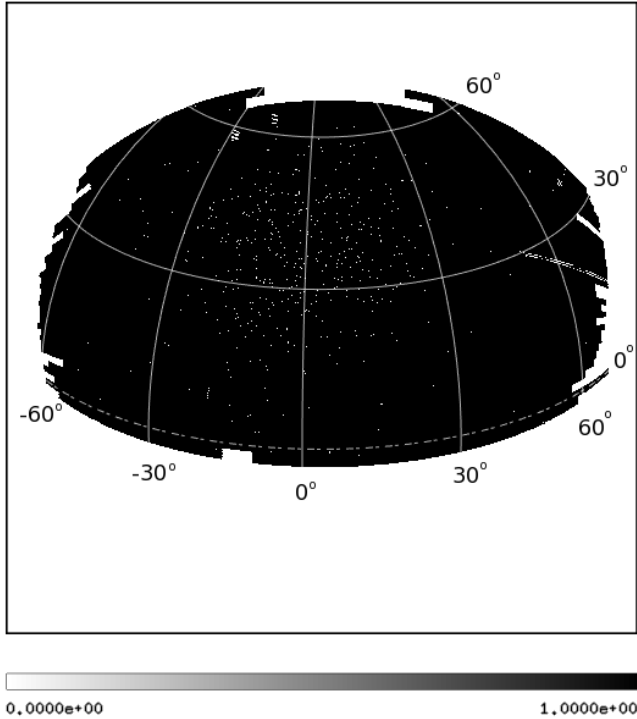


Figure 4. Mask used in the analysis, as described in Section 6.3.

with the MegaZ footprint mask is upgraded to $N_{side}=8192$ for use in our analysis, and is shown in Figure 4.

7 METHOD

To maximize our signal to noise in measuring the average mass profiles of the lenses, we stack the lens galaxies and clusters in bins of richness. The spectroscopic LRG sample is stacked all together, while the cluster catalog is divided into five richness bins, as given in Table 1.

We look around each lens in logarithmic radial bins. In these radial annuli we measure the source counts, average magnitude, and average color, and compare them to the means from the entire source catalog. Using the measured fluctuations in magnitude (δ_m) and counts (δ_c), combined with the α s measured as described above, we calculate Σ_m and Σ_c via equations 11 and 16.

The change in color $g - i$ in annular bins around the lens, compared to the average $g - i$ of the MegaZ LRGs, constitutes our measurement of the reddening $E(g-i)$. This reddening profile can be converted to a measurement of the halo mass profile using equations 17 and 18, with the dust-to-mass fraction Γ as a free parameter.

Our model consists of an NFW profile, BCG profile, a second halo term, and a dust-to-mass ratio. The sum of the first three components yields the total mass density Σ of the lens. The dust-to-mass ratio Γ then relates this Σ to A_i and $E(g-i)$ as described in Section 3. This model $E(g-i)$ is com-

pared directly to our reddening measurements. The model A_i can be used to calculate models for Σ_c and Σ_m using equations 22 and 23, which are compared directly with our measurements of the counts and magnitudes fluctuations.

Measurement errors are determined using jackknife resampling over 133 regions across the survey area. We measure the covariance across radial bins and also between the counts, magnitudes, and reddening measurements. The different richness subsamples are fit independently.

Because our source and lens catalogs span a range of redshifts, Σ_{cr} varies by a factor of nearly 2 over the data set. If we approximate the Σ_{cr} of the sample by its mean, we will smear our results when translating from δ_μ to Σ , the projected mass density of the lens. We therefore divide the analysis into redshift sub-bins of width roughly 0.05, which reduces the difference in Σ_{cr} between neighboring bin pairs to typically 10%. Σ is calculated separately for each pair of foreground/background bins. The final result is obtained by averaging them, weighted by the number of measurements divided by Σ_{cr}^2 .

Our model for the lenses includes six free parameters: M_{200} of the NFW lens halo profile, M_{200} of the cuspy BCG profile, bias b as determined through the second halo term, dust-to-mass fraction Γ , α_c and α_m . The parameters have flat priors except for the α s, which have Gaussian priors with central values and 1σ errors given by the measurements described in section 6.1. We explore the likelihood using Markov Chain Monte Carlo (MCMC) sampling, fitting each richness bin independently.

8 RESULTS

The measured projected mass density profiles Σ_c and Σ_m are shown in Figures 5 through 10 for the LRG sample and the five cluster richness bins, with the counts, magnitudes, and reddening measurements shown separately. The counts and magnitudes results (top left and right, respectively) show the projected mass density profiles $\Sigma_{c,m}$ in units of M_\odot/pc^2 (without the correction for dust extinction), while the reddening measurements (bottom left) show the average $E(B-V)$ in the lens rest frame, calculated from the source model magnitudes $g - i$, the SMC dust model from Pei (1992), and the LRG template `E11_01.sed`. The black data points signify positive values, the red signify negative. The best-fit profiles for the NFW and BCG components are shown in green and blue; the second halo term is shown in purple; the sum of these components is in black. Because our data do not constrain the second halo term well we fix the lens bias, and therefore the second halo term amplitude, as described in Section 8.3. The effects of dust extinction on the counts and magnitudes have been included in the model curves. These corrections decrease the model $\Sigma_{c,m}$, with a stronger effect on Σ_m than on Σ_c . Note that this implies that not only a measurement of reddening, but also a difference in the measurements of Σ_c and Σ_m can constrain Γ .

The bottom-right plots show the counts cross-correlation between the lens and source catalogs, in angular

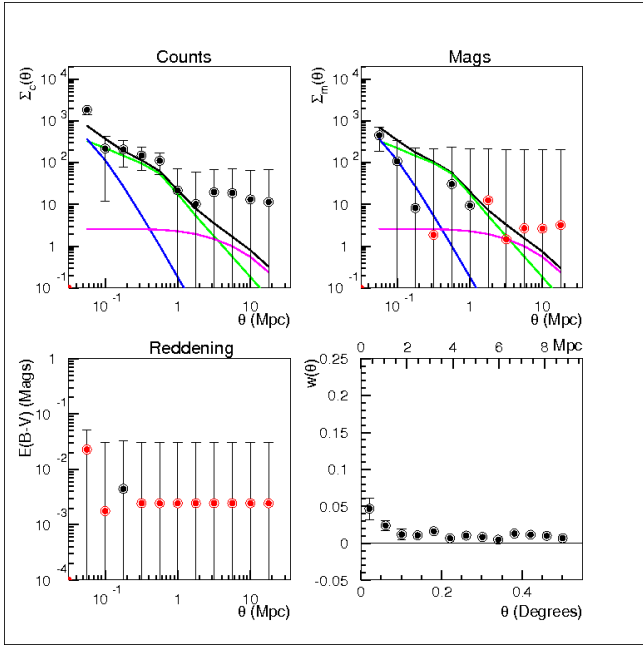


Figure 5. Magnification measured using counts (top left) and magnitudes (top right) for the LRG sample, with units M_{\odot}/pc^2 . Reddening is shown in the bottom left, in units of magnitudes. The cross-correlation between the lenses and sources, in angular bins with units of degrees is shown in the bottom right, with the top-x axis showing the physical scale at the central redshift of the lenses for reference.

Bin	$M_{\text{NFW}} (E14 M_{\odot})$	$M_{\text{BCG}} (E13 M_{\odot})$	$\Gamma (E-6)$
0	$1.26^{+0.30}_{-0.65}$	$1.48^{+0.91}_{-0.79}$	$3.08^{+5.73}_{-3.08}$
1	$1.95^{+0.55}_{-0.82}$	$1.34^{+1.02}_{-0.76}$	$3.76^{+6.85}_{-3.76}$
2	$1.35^{+0.54}_{-0.76}$	$1.60^{+1.33}_{-0.97}$	$6.66^{+6.38}_{-6.66}$
3	$2.57^{+0.83}_{-1.55}$	$3.79^{+2.63}_{-1.87}$	$3.30^{+2.87}_{-3.30}$
4	$4.07^{+2.02}_{-2.32}$	$3.02^{+4.16}_{-1.92}$	$5.94^{+6.66}_{-5.94}$
5	$5.13^{+2.97}_{-4.13}$	$7.82^{+5.03}_{-4.52}$	$8.14^{+8.85}_{-6.02}$

Table 2. Best-fit model parameters with 68% errors. Richness bin, NFW M_{200} , BCG M_{200} , dust-to-mass ratio Γ .

bins, in order to qualitatively compare with the stacking results. Because the catalogs cover a range of redshifts, the correlation function mixes physical scales in its angular bins, causing smaller signal to noise in the cross-correlations than in the stacked results. The x-axis shown on the top of the plot demonstrates, for reference, the scale in Mpc at the central redshift of the lens bin. We measure a significant lensing signal in the inner angular bins that increases with lens richness.

The best-fit model values and 68% errors are given in Table 2 for the NFW and BCG masses and the dust-to-mass ratio Γ .

The correlation matrix for lens richness bin 2 is shown as an example in Figure 11. The matrix contains three main blocks, from left to right (and bottom to top) corresponding to the measurements for counts, magnitudes, and reddening.

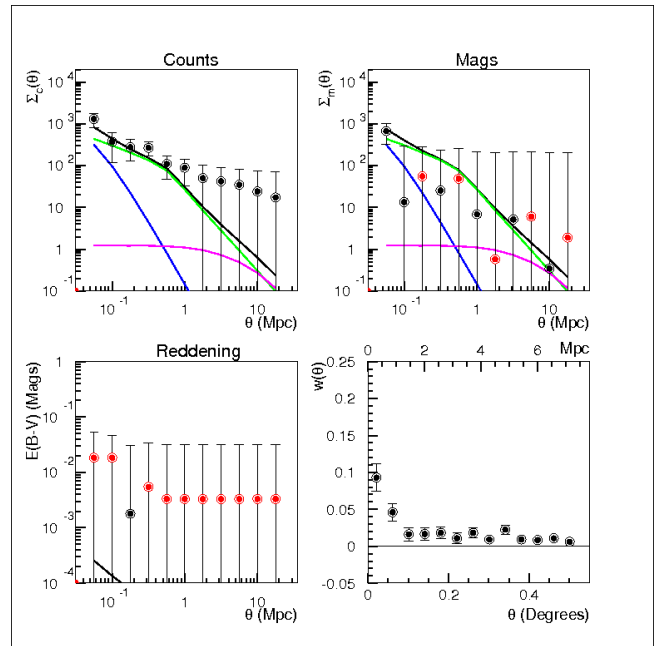


Figure 6. As in Figure 5, for the cluster lens sample with richness 12-17.

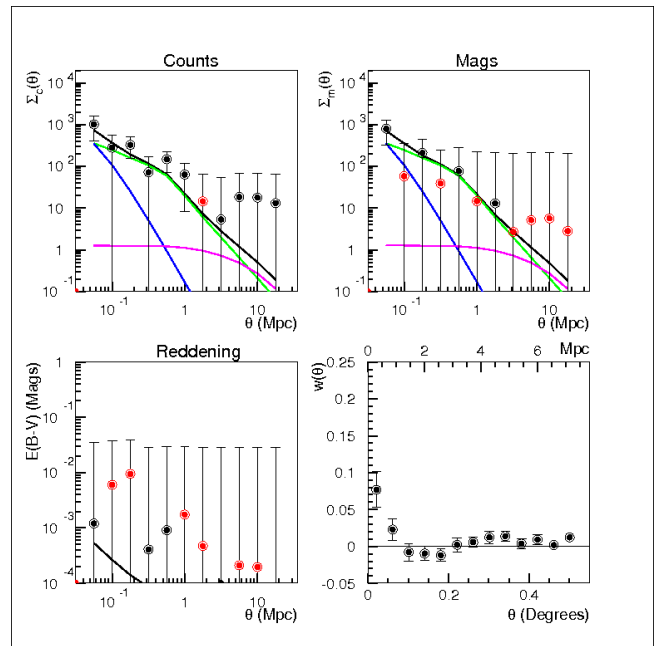


Figure 7. As in Figure 5, for the cluster lens sample with richness 18-25.

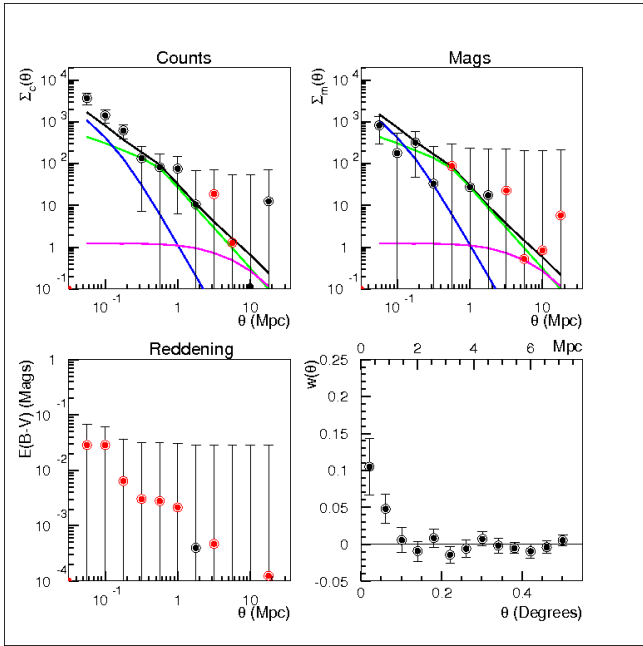


Figure 8. As in Figure 5, for the cluster lens sample with richness 26-40.

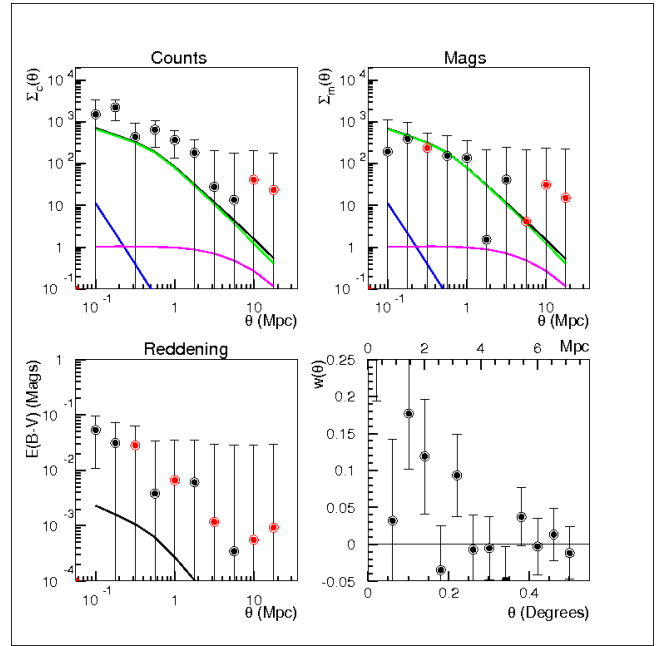


Figure 10. As in Figure 5, for the cluster lens sample with richness 71-220.

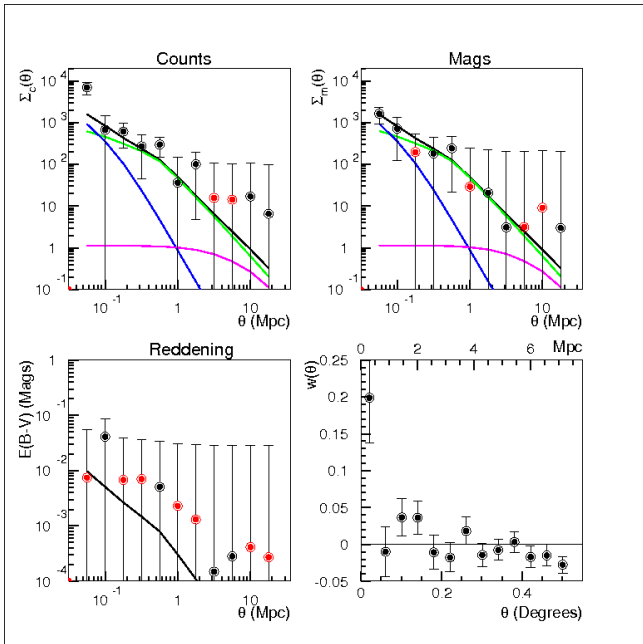


Figure 9. As in Figure 5, for the cluster lens sample with richness 41-70.

ing. The counts, magnitudes, and color measurements are not significantly cross-correlated, indicating that the physical correlation between galaxy luminosity, color, and environment contributes negligible covariance in our analysis.

Note that the correlation between angular bins is much smaller for the magnitudes than for the counts, because the intrinsic spatial correlation of magnitudes has smaller amplitude than that of counts.

8.1 NFW Halo masses

Figure 12 shows the mass M_{200} of the NFW halo, versus richness N . The solid blue line shows the masses measured in previous works, with shading indicating the uncertainty. The cluster mass–richness relation shown is provided in Wen et al. (2012) (WHL12), determined using weak lensing shear and X-ray data. The values plotted for each richness bin are the mean mass expected given the distribution in richness of the clusters in that bin. The LRG measurement is based on the measured bias of this sample of $b=1.85\pm 0.25$, determined using the anisotropic correlation function $\xi(\sigma, \pi)$ in Cabré & Gaztañaga (2009) (CG09). This bias can be converted to a halo mass according to Tinker et al. (2010), resulting in a mass of $3.5^{+1.8}_{-1.4} E13 M_{\odot}$. Assuming a finite mass range with upper limit given by the smallest cluster halo mass, compared to assuming a narrow mass bin, only changes the mass estimate by $1E12 M_{\odot}$.

The four sets of data points show the fit results using all data (black squares), Σ_c and Σ_m ignoring dust extinction effects (red right-facing triangles), only Σ_m (gray up-facing triangles), and only Σ_c (green down-facing triangles). The

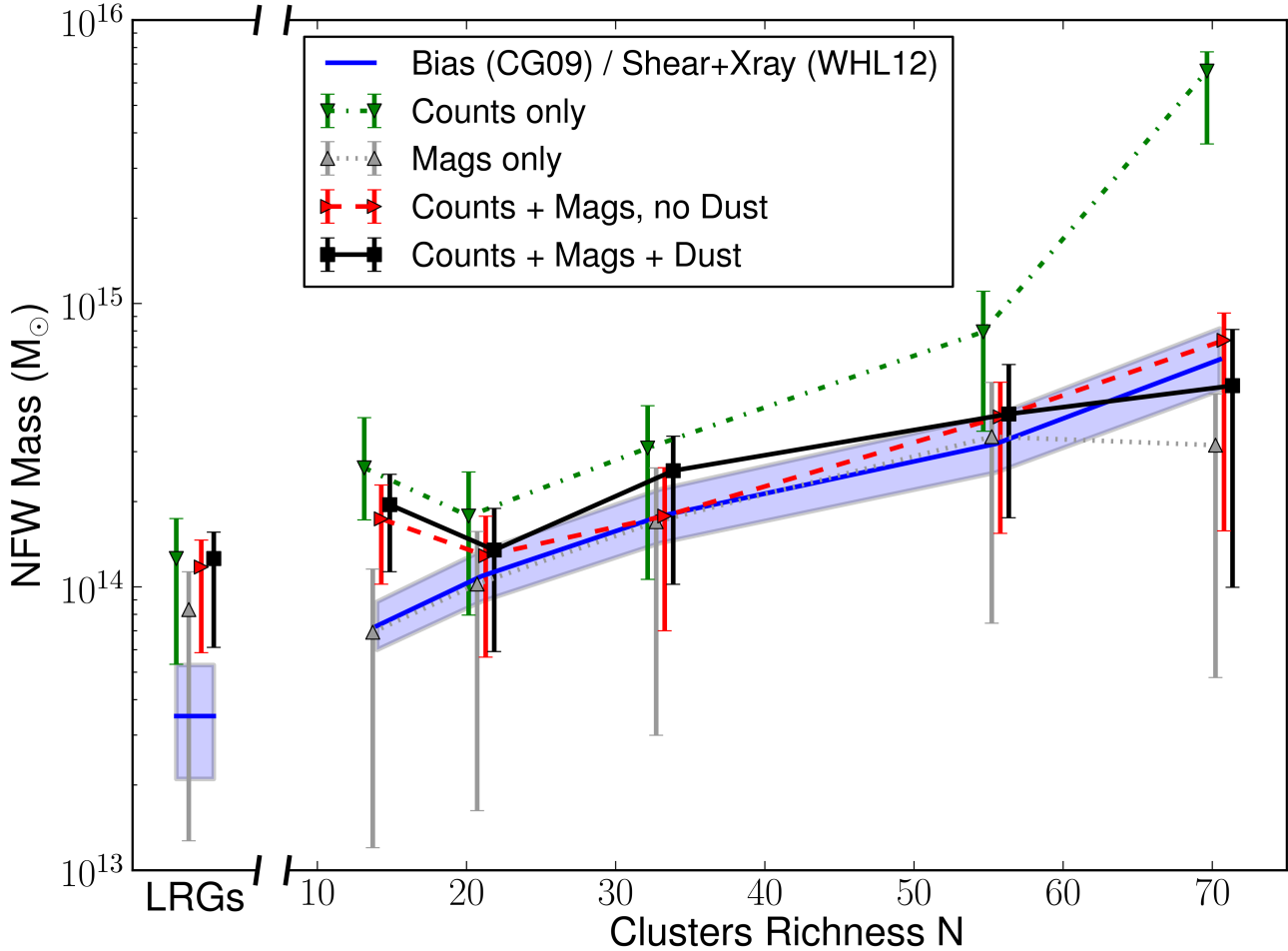


Figure 12. Mass-Richness relation for the main NFW halo, compared to the shear and X-ray results given in WHL12 and to the bias results from CG09. Different data points represent different combinations of data included in the fit.

results are mainly consistent; however, fitting only Σ_c systematically leads to a larger best-fit halo mass. The Σ_m -only results have very large error bars, as expected from the systematic photometry errors in the data. The plot points are slightly offset in the x direction for clarity.

8.2 Dust-to-mass fraction

Table 2 lists the best-fit dust-to-mass ratio Γ for the different richness bins. The measurements are consistent with zero, and are therefore upper limits. The 3σ upper limits for the richness bins are $[2.5, 2.9, 3.7, 1.9, 3.4, 5.5] \times 10^{-5}$. The best-fit values imply a small dust correction to the mass density profile Σ ; for our most massive lens bin the dust reduces Σ_c and Σ_m by less than 5%.

8.3 Lens bias

We fit the amplitude of the second halo term as parameterized by the bias of the lens. As the signal to noise is very low in the angular range where the second halo term dominates, we do not find interesting constraints on the bias. The different bins' best-fit biases are similar, with 1σ uncertainties ranging between biases of typically 2 to 9. A large bias corresponds to a small second halo term; our best-fit biases trend high because the signal at large radii is consistent with zero. As we do not constrain well the bias, we rerun the analysis with a fixed value of $b = 3.0$ for the clusters and $b = 2.0$ for the LRGs, and find almost identical results for the remaining fit parameters. These are the results shown in Table 2 and Figures 5-10.

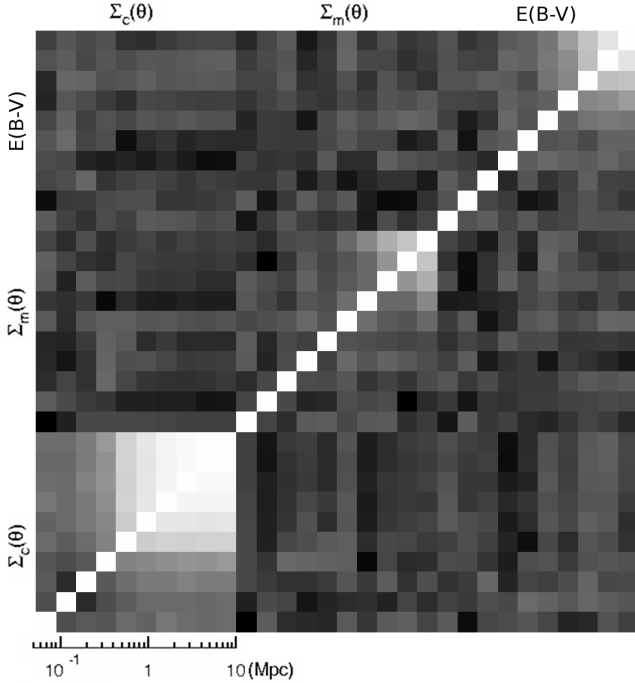


Figure 11. Correlation matrix for cluster richness bin 2. The three blocks are for counts, magnitudes, and reddening (from left to right and bottom to top).

8.4 Systematic Checks

8.4.1 Intrinsic correlations

The MegaZ LRG sample’s redshifts are estimated using photometry, which at times leads to significant redshift error. Because MegaZ is selected using the same criteria as the 2SLAQ spectroscopic sample, the photometric redshift errors in MegaZ can be quantified reliably. The true redshift distribution $N(z)$ of the 2SLAQ sample is compared in detail with the photo- z distribution for the MegaZ catalog, as calculated with BPZ, in Martí et al. (2013). A fit to the distribution, consisting of four Gaussian profiles, is shown in Figure 1. We use this fit to estimate the fraction of the MegaZ sample that lies below redshift 0.4, therefore overlapping the lens sample, taking into account the error on the Gaussian parameters. We find an overlap rate of 0.012 ± 0.001 .

To assess the level of contamination in the magnification signal due to this overlap, we perform the analysis replacing the MegaZ data with a sample of LRGs with spectroscopic redshifts $0.3 < z < 0.4$. For this “overlap” sample we use the same catalog used for the LRG lenses, but limited to this redshift range, which as seen in Figure 1 is the redshift region with significant overlap between the samples. As the MegaZ is an LRG catalog, we expect our LRG spectroscopic galaxies to have similar clustering properties to the MegaZ’s redshift outlier LRGs. More importantly, this overlap sample strongly correlates spatially with our lenses, as would be

expected for any outlier MegaZ galaxies in our source sample that lie in this lower redshift range. As a result, when we perform our stacking analysis using this overlap sample we find a strong signal reflecting the intrinsic correlation in counts, magnitudes, and color for galaxies spatially close to the lenses. This spurious signal rises as the galaxies’ angular separation decreases, qualitatively similarly to the lensing signal. As this spurious signal indicates the strength of the correlation for a completely overlapping redshift sample, we multiply by the overlap fraction of 0.012 to determine the amount of signal in our stacking analysis that is due to the overlapping fraction of sources. We note that this scaling by 0.012 simply scales the total fraction of outlier sources; the effects of increased contamination as one approaches the lenses is preserved in our estimate of the intrinsic correlations. The resulting contamination is small: less than 0.3 times the error bars in Σ_c , 0.05 times the error bars in Σ_m , and 0.02 times the error bars in $E(B-V)$. We could subtract the intrinsic contribution from the magnification data; however, there are significant error bars on the intrinsic measurements that would add to the analysis’ covariance. Because the effect is not significant compared to the current measurement errors we therefore ignore it in the analysis. In future work with better precision, the intrinsic overlap may play an important role.

8.4.2 NFW concentration relation

As a check to ensure that our results are not sensitive to our assumptions about the NFW halo concentration, we perform the analysis again using the concentration relation from Duffy et al. (2008):

$$c(M_{200}, z) = 5.71 \left(\frac{M_{200}}{2 \times 10^{12} h^{-1} M_{\odot}} \right)^{-0.084} (1+z)^{-0.47}. \quad (29)$$

Our results are consistent with those using the concentration from Mandelbaum et al. (2008). In most cases the NFW and BCG best-fit masses change by less than 10%, and in all cases well within the 1σ errors. Changing the concentration relation causes the best-fit masses to increase in some bins and decrease in others, and does not have a coherent effect on the results.

8.4.3 Miscentering

Our implementation of the NFW halo fit includes the effects of halo miscentering as parameterized by Johnston et al. (2007), assuming a probability of miscentering that depends on the halo richness. We remove the miscentering correction and repeat the analysis to quantify its influence on our results. For reference, the effect of miscentering on the model NFW profile is shown in Figure 13, in which is plotted the NFW profile mass density Σ including the contribution from miscentering, divided by the NFW profile Σ corresponding to the same halo mass without a miscentering contribution. The different lines represent the best-fit NFW masses for our six richness bins, showing that miscentering tends to

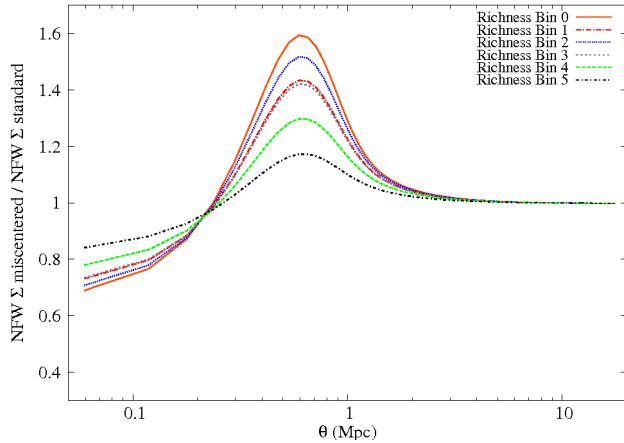


Figure 13. Model projected mass density Σ of the best-fit NFW profile including miscentering effects, divided by the NFW profile with identical mass without miscentering. The different lines correspond to the best-fit profiles for different richness bins.

most strongly affect the least massive haloes. Miscentering decreases the mass density profile at small radii by several tens of percent, and increases Σ at intermediate radii by up to $\sim 50\%$, causing an overall flattening of the profile shape. The effect can be quite strong, but the decrement at low radii counters the increment at intermediate radii such that the total NFW fits are not significantly altered. We find that without miscentering, our best-fit NFW masses change by typically $\sim 10\%$, in some bins increasing and in others decreasing. The BCG best-fit masses do show a coherent response, decreasing to typically 70-75% their original values. Qualitatively, this behavior is expected because the BCG contribution is significant only on scales where miscentering decreases the NFW profile, and therefore removing miscentering will increase the inner NFW Σ and lessen the need for a BCG mass contribution. Quantitatively, the change is within the BCG M_{200} 1σ measurement errors in all bins.

9 DISCUSSION AND CONCLUSIONS

We measure the effects of gravitational lensing magnification on the MegaZ catalog, a photometric sample of LRGs from SDSS DR7. We study the effects of gravitational lensing on the detected number counts of sources and also the average brightness of sources behind lenses compared to the average values in the source catalog. As lenses, we use the WHL12 catalog of galaxy clusters detected in SDSS DR9 (Wen et al. 2012), and also a spectroscopic sample of LRGs selected from SDSS DR6.

We fit the lens NFW halo mass, BCG mass, lens bias, and dust-to-mass ratio in six bins of richness. We measure a NFW mass vs. cluster richness relation that is consistent with that given in Wen et al. (2012) from weak lensing shear and X-ray data. Fitting only the counts magnification data, without including flux magnification or taking into account

reddening measurements, yields systematically larger masses that are in worse agreement with the previous results.

The fit to our lens model is performed between the radial range of 0.04 Mpc to 13 Mpc. Below roughly 0.04 Mpc we expect the foreground lens galaxy (the LRG or the cluster BCG) to obstruct the observations of background galaxies, adversely affecting the accuracy of the detection and photometry of the sources (Mandelbaum et al. 2006). Such data reduction difficulties due to galaxy proximity and crowded fields are not fully understood, and likely bias our results at small radii from the lens. These uncertainties will most strongly affect the best-fit BCG masses; therefore, we note that we expect that the BCG model fits are significantly affected by this systematic error. For example, the best-fit BCG masses using the Σ_c data alone range from $2.2e13$ to $4.4e14$, indicating a discrepancy in the Σ_c and Σ_m data (as expected since data systematics affect the different probes differently; see Mandelbaum et al. 2006) and yielding in this case values that are unphysically massive. It is possible that such systematics also contribute to the discrepancy in NFW halo mass when fitting only Σ_c compared to the full data set. Our results therefore stress the value of multiple probes in analyses of public data where the image reduction can not be fully explored and optimized for each science case.

In addition to measuring the change in number counts and brightness, we measure the change in color of sources behind lenses in order to measure reddening of the objects due to dust in the lens systems. Dust extinction serves to redden the sources and also make them appear fainter; the change in flux due to dust is therefore degenerate with the change in flux due to lensing. The degeneracy can be broken through the color dependence of dust extinction, as lensing magnification is achromatic.

We find no significant reddening of the lensed sources, yielding upper limits on the dust-to-mass ratios of the lenses. The systematic errors in the SDSS photometry are large enough to obscure the small color changes expected due to dust extinction. To improve on these measurements we will have to be extremely careful about quantifying systematic errors in the photometry, as percent-level shifts can arise from (for example) background subtraction errors in crowded fields⁷. As our cluster lenses themselves constitute crowded fields, the amplitude of such photometric errors in source magnitudes can be spatially correlated with the galaxy lens positions.

Previous studies imply dust-to-mass ratios for LRGs consistent with our upper limits. Barber et al. (2007) selected LRGs from SDSS DR4 with the same criteria as our LRG lens sample, which was selected from SDSS DR6. Their population synthesis analysis of the sample determined a median extinction in the z band of $A_z = 0.0026$; this measurement implies $E(B-V) \sim 0.001$ (much smaller than our systematic color error of 0.02), and dust-to-mass ratio $\Gamma = 1e-06$, assuming our LRG lens best-fit mass. Tojeiro et al. (2009) used the VESPA algorithm to determine a typical

⁷ <http://www.sdss.org/dr7/products/images/index.html#skylevz>

V-band optical depth $\tau_V < 0.2$ due to dust in the interstellar medium of SDSS spectroscopic LRGs in SDSS DR7, also selected identically to our LRG lens sample. As optical depth $\tau_V = \ln(10)/2.5 A_V$, we can convert this τ_V limit to an $E(B-V) < 0.06$, and to a dust-to-mass ratio $\Gamma < 8e-5$. Using quasar magnification and reddening, Ménard et al. (2010) found a dust-to-mass ratio in the main galaxy sample of SDSS to be roughly $1e-5$; as the galaxy sample they studied is expected to be more dusty on average than LRGs, we would expect this to be an upper limit of the dust content in our lenses. We find 3σ upper limits for the dust-to-mass ratios in the range of 2 to 6 e-5 for the different richness bins, in good agreement with expectations for single LRGs. We do not find significant evidence for a change in dust-to-mass ratio with lens richness. It is expected that cluster environments are less dusty than individual galaxies (Chelouche et al. 2007; Muller et al. 2008); as our results place only upper limits on the dust fraction, we can not support or refute this claim.

Photometric LRGs are a convenient sample to study as they are numerous, bright, and have similar intrinsic colors. Their homogenous color is advantageous for two reasons: it decreases the noise in the $g - i$ reddening measurements, and it causes LRGs to be well-suited to photometric redshift estimation. Knowledge of the photometric redshift error is essential in studies of gravitational lensing magnification, as the presence of photo-z outliers can mimic the lensing signal. The existence of a spectroscopic galaxy sample that is representative of the photometric catalog, as 2SLAQ is for the MegaZ data set, is crucial for understanding the true redshift distribution of the photometric galaxies. Because of these data we can measure very precisely the fraction of overlap between our source and lens samples, and therefore constrain the contribution of intrinsic overlap to our lensing signal. In the current analysis, such intrinsic correlation is small compared to the statistical error in the measurements. It is important, however, that we are able to quantify the contribution.

The signal to noise of the lensing-induced counts overdensity is larger than that of the average flux increase of the lens sample. Although we do measure significant magnitude magnification signal, it is typically in the inner angular regions that are dominated by the BCG. The upper limits on the magnitude magnification, however, do yield a constraint on the mass profiles of the lenses. This effect is most strongly seen in the highest richness bin, where the counts alone yield a significantly higher best-fit NFW mass than the combined fit with magnitudes, or with magnitudes and dust. (All three results give a good χ^2 fit to the data.) Although the signal to noise of the change in counts is larger than that of the change in magnitudes, the factors that convert these basic measurements into mass density profiles are better constrained for magnitudes magnification than for counts. For example, the uncertainty on alpha is six times larger for counts due to the higher intrinsic correlation of counts compared to magnitudes. For the same reason, the covariance between angular bins is much higher in the mass profile

measured using counts, compared to using magnitudes. Because of these considerations, relatively poor measurements of magnitude magnification can still yield an important constraint on the lens mass profiles. The contribution of magnitude and reddening measurements to the best-fit NFW halo masses, despite the low signal to noise of the measurements, indicates the importance of including these probes in weak lensing magnification analyses.

This is the first analysis to simultaneously fit the magnification effects on number counts and magnitudes as well as reddening due to dust in order to constrain the mass profiles and dust content of a lens sample. In addition, this work uses as its source sample a catalog of photometric LRGs, which is a bright galaxy population that is numerous and easily-detected in typical survey data. We present significant measurements of the mass profiles of our LRG and galaxy cluster lenses that are in good agreement with previous estimates using different techniques. The quality of our measurements is currently limited by the photometric error in the source catalog. Upcoming projects such as the Dark Energy Survey (DES)⁸, Hyper Suprime-Cam Survey (HSC)⁹, and the Large Synoptic Survey Telescope (LSST)¹⁰ will produce vast galaxy catalogs with high-quality photometry on which we can apply these analysis techniques to study lensing magnification with unprecedented precision.

ACKNOWLEDGMENTS

We thank Arnau Pujol for help relating the halo mass with the bias of the LRG lens sample. We acknowledge the support of the JAE-Doc (CSIC) fellowship, the Spanish Science Ministry AYA2009-13936, AYA2012-39559, Consolider-Ingenio CSD2007-00060, project 2009SGR1398 from Generalitat de Catalunya, the Marie Curie European Reintegration Grant PERG07-GA-2010-268290, and the European Commission Marie Curie Initial Training Network Cosmo-Comp (PITN-GA-2009-238356)

REFERENCES

- Abazajian K., Adelman-McCarthy J. K., Agüeros M. A., Allam S. S., Anderson K. S. J., Anderson S. F., et al., 2005, *The Astronomical Journal*, 129, 1755
- Abazajian K. N., et al., 2009, *ApJS*, 182, 543
- Adelman-McCarthy J. K., et al., 2008, *ApJS*, 175, 297
- Barber T., Meiksin A., Murphy T., 2007, *MNRAS*, 377, 787
- Bauer A. H., Baltay C., Ellman N., Jerke J., Rabinowitz D., Scalzo R., 2012, *The Astrophysical Journal*, 749, 56
- Bauer A. H., Seitz S., Jerke J., Scalzo R., Rabinowitz D., Ellman N., Baltay C., 2011, *The Astrophysical Journal*, 732, 64

⁸ <http://www.darkenergysurvey.org>

⁹ <http://www.naoj.org/Projects/HSC>

¹⁰ <http://www.lsst.org>

- Benítez N., 2000, *The Astrophysical Journal*, 536, 571
- Cabré A., Gaztañaga E., 2009, *MNRAS*, 393, 1183
- Cannon R., Drinkwater M., Edge A., Eisenstein D., Nichol R., Outram P., Pimblett K., de Propris R., Roseboom I., Wake D., Allen P., Bland-Hawthorn J., Bridges T., Carson D., Chiu K., Colless M., Couch W., Croom S., Driver S., Fine S., Hewett P., Loveday J., Ross N., Sadler E. M., Shanks T., Sharp R., Smith J. A., Stoughton C., Weilbacher P., Brunner R. J., Meiksin A., Schneider D. P., 2006, *MNRAS*, 372, 425
- Chelouche D., Koester B. P., Bowen D. V., 2007, *The Astrophysical Journal*, 671, L97
- Coupon J., Broadhurst T., Umetsu K., 2013, *The Astrophysical Journal*, 772, 65
- Duffy A. R., Schaye J., Kay S. T., Dalla Vecchia C., 2008, *MNRAS*, 390, L64
- Ford J., Hildebrandt H., Van Waerbeke L., Erben T., Laigle C., Milkeraitis M., Morrison C., 2013, *ArXiv e-prints*
- Ford J., Hildebrandt H., Van Waerbeke L., Leauthaud A., Capak P., Finoguenov A., Tanaka M., George M. R., Rhodes J., 2012, *The Astrophysical Journal*, 754, 143
- Gaztañaga E., 2003, *The Astrophysical Journal*, 589, 82
- Górski K. M., Hivon E., Banday A. J., Wandelt B. D., Hansen F. K., Reinecke M., Bartelmann M., 2005, *The Astrophysical Journal*, 622, 759
- Hildebrandt H., Muzzin A., Erben T., Hoekstra H., Kuijken K., Surace J., van Waerbeke L., Wilson G., Yee H. K. C., 2011, *The Astrophysical Journal*, 733, L30
- Hildebrandt H., van Waerbeke L., Scott D., Béthermin M., Bock J., Clements D., Conley A., Cooray A., Dunlop J. S., Eales S., Erben T., Farrah D., Franceschini A., Glenn J., Halpern M., Heinis S., Ivison R. J., Marsden G., Oliver S. J., Page M. J., Pérez-Fournon I., Smith A. J., Rowan-Robinson M., Valtchanov I., van der Burg R. F. J., Vieira J. D., Viero M., Wang L., 2013, *MNRAS*, 429, 3230
- Huff E. M., Graves G. J., 2011, *ArXiv e-prints*
- Johnston D. E., Sheldon E. S., Wechsler R. H., Rozo E., Koester B. P., Frieman J. A., McKay T. A., Evrard A. E., Becker M. R., Annis J., 2007, *ArXiv e-prints*
- Mandelbaum R., Seljak U., Cool R. J., Blanton M., Hirata C. M., Brinkmann J., 2006, *MNRAS*, 372, 758
- Mandelbaum R., Seljak U., Hirata C. M., 2008, *JCAP*, 8, 6
- Mandelbaum R., Tasitsiomi A., Seljak U., Kravtsov A. V., Wechsler R. H., 2005, *MNRAS*, 362, 1451
- Mantz A., Allen S. W., Ebeling H., Rapetti D., 2008, *MNRAS*, 387, 1179
- Martí P., Miquel R., Bauer A., Gaztañaga E., 2013, *ArXiv e-prints*
- Ménard B., Scranton R., Fukugita M., Richards G., 2010, *MNRAS*, 405, 1025
- Morrison C. B., Scranton R., Ménard B., Schmidt S. J., Tyson J. A., Ryan R., Choi A., Wittman D. M., 2012, *MNRAS*, 426, 2489
- Muller S., Wu S.-Y., Hsieh B.-C., González R. A., Loinard L., Yee H. K. C., Gladders M. D., 2008, *The Astrophysical Journal*, 680, 975
- Navarro J. F., Frenk C. S., White S. D. M., 1997, *ApJ*, 490, 493
- Pei Y. C., 1992, *The Astrophysical Journal*, 395, 130
- Press W. H., Schechter P., 1974, *The Astrophysical Journal*, 187, 425
- Rozo E., Wechsler R. H., Rykoff E. S., Annis J. T., Becker M. R., Evrard A. E., Frieman J. A., Hansen S. M., Hao J., Johnston D. E., Koester B. P., McKay T. A., Sheldon E. S., Weinberg D. H., 2010, *The Astrophysical Journal*, 708, 645
- Schmidt F., Leauthaud A., Massey R., Rhodes J., George M. R., Koekemoer A. M., Finoguenov A., Tanaka M., 2012, *The Astrophysical Journal*, 744, L22
- Schneider P., King L., Erben T., 2000, *Journal of Astronomy and Astrophysics*, 353, 41
- Schneider P., Kochanek C., Wambsgans J., 2004, *Saas-Fee Advanced Courses*, Vol. 33, *Gravitational Lensing: Strong, Weak and Micro*, Meylan G., Jetzer P., North P., eds. Springer, Berlin, Germany; New York, U.S.A.
- Scoccimarro R., Sheth R. K., Hui L., Jain B., 2001, *The Astrophysical Journal*, 546, 20
- Scranton R., Ménard B., Richards G. T., Nichol R. C., Myers A. D., Jain B., Gray A., Bartelmann M., Brunner R. J., Connolly A. J., Gunn J. E., Sheth R. K., Bahcall N. A., Brinkman J., Loveday J., Schneider D. P., Thakar A., York D. G., 2005, *The Astrophysical Journal*, 633, 589
- Sheth R. K., Tormen G., 1999, *MNRAS*, 308, 119
- Sonnenfeld A., Bertin G., Lombardi M., 2011, *Journal of Astronomy and Astrophysics*, 532, A37
- Thomas S. A., Abdalla F. B., Lahav O., 2010, *ArXiv e-prints*
- Tinker J. L., Robertson B. E., Kravtsov A. V., Klypin A., Warren M. S., Yepes G., Gottlöber S., 2010, *The Astrophysical Journal*, 724, 878
- Tojeiro R., Wilkins S., Heavens A. F., Panter B., Jimenez R., 2009, *ApJS*, 185, 1
- Umetsu K., Medezinski E., Nonino M., Merten J., Zitrin A., Molino A., Grillo C., Carrasco M., Donahue M., Mahdavi A., Coe D., Postman M., Koekemoer A., Czakon N., Sayers J., Mroczkowski T., Golwala S., Koch P. M., Lin K.-Y., Molnar S. M., Rosati P., Balestra I., Mercurio A., Scodreggio M., Biviano A., Anguita T., Infante L., Seidel G., Sendra I., Jouvel S., Host O., Lemze D., Broadhurst T., Meneghetti M., Moustakas L., Bartelmann M., Benítez N., Bouwens R., Bradley L., Ford H., Jiménez-Teja Y., Kelson D., Lahav O., Melchior P., Moustakas J., Ogaz S., Seitz S., Zheng W., 2012, *The Astrophysical Journal*, 755, 56
- Van Waerbeke L., Hildebrandt H., Ford J., Milkeraitis M., 2010, *The Astrophysical Journal*, 723, L13
- Weingartner J. C., Draine B. T., 2001, *The Astrophysical Journal*, 548, 296
- Wen Z. L., Han J. L., Liu F. S., 2012, *The Astrophysical Journal*, 199, 34